# Multi-View 3D Modeling of Large Objects for Robotic Piercing on Unknown Free-Form Surfaces

Chun-An Liu, Chih-Hsien Yen, Hung-Xian Wu, Kai-Tai Song, Fellow, RST, and Chin-Chi Hsiao

Abstract—This paper presents a method for 3D modeling of unknown large objects using a depth camera and executing holepiercing operations at specified target locations on the modeled surface. To address the limitations of single-viewpoint perception, a mobile manipulator equipped with a depth camera adopts a multi-view point cloud acquisition strategy. The proposed method fuses multi-view point cloud data by using Iterative Closest Point (ICP) registration, combined with outlier removal and smoothing techniques, to generate an accurate and complete 3D model. To further improve segmentation and object isolation, DBSCAN clustering is applied. The experimental platform includes a 3D LiDAR installed on the mobile base for mapping the environment, while point clouds from the depth camera are aligned to a global coordinate system. Experimental result shows that the root mean square error (RMSE) of 3D modeling of a box-shaped object is 7.84 mm. Based on the reconstructed model, automated piercing operations on two large objects have been demonstrated using the mobile manipulator. This multi-view 3D reconstruction framework allows for vision-based automated reconstructing and machining of large, unknown surfaces.

Index Terms—3D modeling, point cloud, data fusion, robot control.

#### I. INTRODUCTION

In modern manufacturing, automated machining of large, unstructured, and previously unknown objects poses significant challenges, particularly in perception and modeling. Traditional single-viewpoint depth cameras often suffer from occlusions and missing data, resulting in incomplete 3D representation. To overcome this limitation, we propose a mobile robotic system that leverages multi-viewpoint point cloud fusion for complete object modeling and tool path generation.

In the context of 3D object modeling using visual sensing, depth cameras are commonly employed to acquire point cloud data. Due to inevitable sensor noise, Gaussian distribution-based methods[1][2], such as those in the Point Cloud Library (PCL) [3], are often used to remove outliers and sparse points surrounding the object, thereby improving the quality of the point cloud. A typical denoising process involves computing the average distance between each point and its nearest neighbors,

Research supported in part by National Science and Technology Council of Taiwan R.O.C under grant NSTC 113-2218-E-A49-002 – and Industrial Technology Research Institute (ITRI).

Kai-Tai Song, Chun-An Liu, Chih-Hsien Yen and Hung-Xian Wu are with the Institute of Electrical and Control Engineering, College of Electrical and Computer Engineering, National Yang Ming Chiao Tung University, Hsinchu, Taiwan R.O.C. (e-mail:ktsong@nycu.edu.tw; ca4488she.ee12@nycu.edu.tw; sam8899yy.ee12@nycu.edu.tw; abcwu11111.ee12@nycu.edu.tw.)

Chin-Chi Hsiao is with Intelligent Robotics Technology Division, Mechanical and Mechatronics Systems Research Labs, Industrial Technology Research Institute (ITRI), Taiwan R.O.C. (e-mail:hsiao\_cc@itri.org.tw)

Manuscript received 11 September 2025; accepted 11 October 2025; Date of publication 12 November 2025.

followed by calculating the global mean and standard deviation

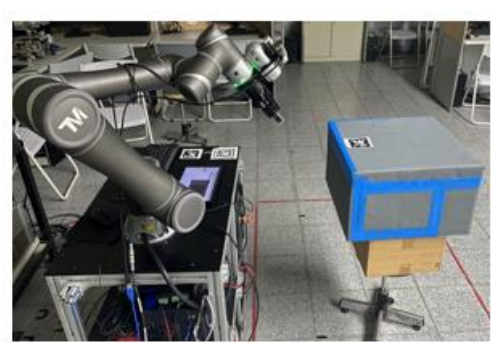


Fig. 1. System set up for multi-view point cloud sampling.

of all average distances. Points falling outside a user-defined range based on mean and standard deviation are then removed [1]. For more complex scenes, clustering algorithms like KD-Tree [3] are applied to segment point clouds into meaningful object groups. Harintaka *et al.* [4] explored automated segmentation of point clouds acquired from low-cost terrestrial laser scanner. To overcome the inefficiency and inaccuracy of manual processing, they proposed a hybrid method combining RANSAC for initial planar segmentation (walls, floors, ceilings) and DBSCAN for refining and reassigning misclassified points. The resulting segmentation distinguishes structural and interior elements effectively. Furthermore, graph-based methods have been used for efficient and accurate point cloud segmentation [5].

For large-scale object modeling, prior works often adopt a scan-then-plan strategy. Maboudi *et al.* [6] proposed a view planning method based on online reconstruction. Their approach incrementally reconstructs the object while continuously assessing model quality to identify poorly reconstructed surfaces. Viewpoints are planned iteratively to maximize surface coverage and reconstruction fidelity. This integration of online reconstruction and view planning addresses key limitations of traditional offline strategies.

Point cloud incompleteness remains a critical issue in vision-based 3D applications. Recent studies have leveraged deep learning for point cloud completion. Ben *et al.* [7] reviewed a range of approaches including point-based, view-based, convolution-based, graph-based, and generative model-based methods. These approaches aim to predict missing regions of incomplete 3D shapes. However, the unordered nature of point clouds challenges the generation of fine-grained structures. To address this, Xin *et al.* [8] reformulated the completion task as a deformation process, allowing the model to more accurately capture the geometry of the missing regions.

This work aims to address the needs of hole-piercing on large free-form objects where visual modeling must be robust to environmental complexity and surface irregularity. The multi-

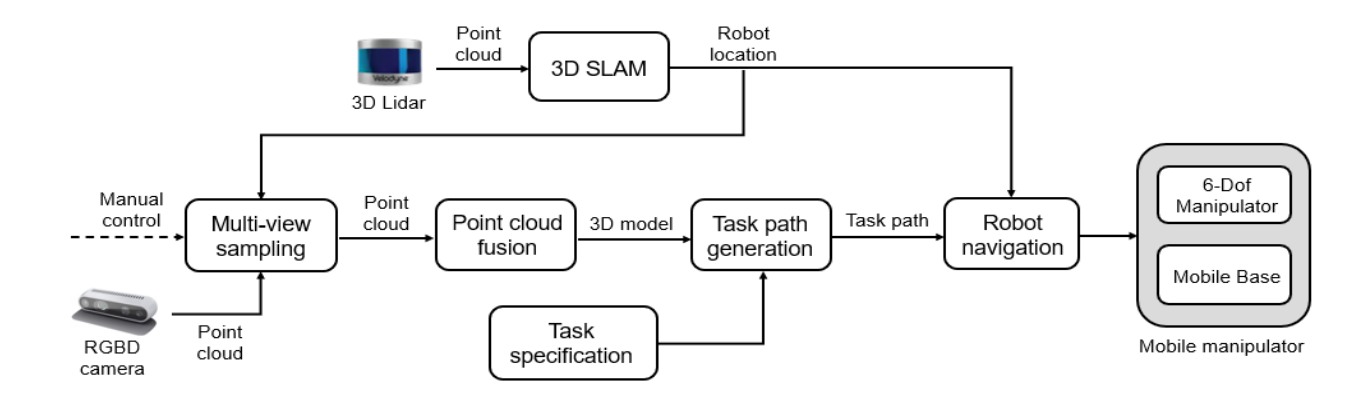


Fig. 2. Proposed system architecture.

view fusion process is divided into two stages: (1) multi-angle point cloud sampling and (2) registration and segmentation to extract usable geometry. Through this approach, we construct high-fidelity models that form the basis for reliable, vision-guided robotic piercing operations. The system is built around a mobile manipulator with a depth camera mounted in an eye-in-hand configuration as shown in Fig. 1. A 3D LiDAR sensor is fixed to the mobile base to build a global 3D map of the environment. All acquired point clouds are transformed into a unified global coordinate frame to facilitate localization and consistent data integration. The core of our system lies in fusing point clouds captured from multiple views using Iterative Closest Point (ICP) [9] registration, enhanced by noise removal and smoothing techniques. This process mitigates occlusion effects and data loss.

To ensure segmentation of the target object from the environment, we apply Density-Based Spatial Clustering of Applications with Noise (DBSCAN). The reconstructed point cloud model is then used to generate piercing paths tailored to the object's geometry. In our experimental validation, AprilTag markers are employed to localize targets on the modeled surface, ensuring alignment between the virtual model and the physical object.

The rest of the paper is organized as follows. Section II introduces the architecture of the proposed multi-view 3D modeling and task path planning system. Section III describes the method for multi-view point cloud fusion. Section IV details the point cloud-based robotic hole-piercing tasks. Section V presents several experiments conducted to verify the effectiveness of the proposed system. Finally, the conclusions are given in Section VI.

#### II. PROPOSED SYSTEM ARCHITECTURE

The system architecture of the proposed multi-view 3D modeling and task-path generation method is illustrated in Fig. 2. The system consists of two main layers: the perception layer and the task execution layer. In the perception layer, a 3D LiDAR sensor is employed to capture large-scale environmental point cloud data. This data is fed into a 3D SLAM (Simultaneous Localization and Mapping) module, which constructs a map of the environment and continuously estimates the pose of the mobile platform. This ensures accurate localization and global spatial awareness for the robotic system.

In parallel, an RGB-D camera mounted on the end-effector of a robotic manipulator is utilized to capture high-resolution, object-focused depth images from multiple viewpoints. These multi-view depth data are converted into partial point clouds, which are then registered through a point cloud alignment pipeline to form a unified and complete 3D model of the target object. This reconstruction process accounts for occlusions and sensor noise, enabling accurate representation of the object geometry. Based on the reconstructed 3D model, a path planning module generates piercing trajectories tailored to the geometry of the object. These paths are specifically designed to support robotic hole-piercing operations. The computed trajectories are then transmitted to the robot controller, which executes the piercing operation and completes the automated task.

#### III. MULTI-VIEW POINT CLOUD FUSION

The modeling process is divided into two parts: multi-view point cloud sampling and object model extraction. Multi-view point cloud sampling uses the eye-in-hand camera on the mobile robot to obtain the current observation point cloud, and samples it in the same coordinate system through coordinate conversion. After obtaining multiple frames of point clouds sampled from different perspectives, object model extraction overlaps the point clouds of different perspectives in each frame to obtain a complete observation point cloud, and then segments the object to extract the target model.

# A. Multi-View Point Cloud Sampling:

During the point cloud sampling stage, the mobile manipulator is manually teleoperated to move around the target object, capturing a series of point clouds from different viewpoints along with the corresponding pose information, as illustrated in Fig. 3. The recorded transformation matrices of each sampling pose are used to provide initial alignment for subsequent ICP-based registration.

In the current design, AprilTag markers are attached to the workpiece and are used for secondary positioning in subsequent tasks. This mechanism enables the recalibration of the relative position between the mobile manipulator and the workpiece. In scenarios where the distance between the workpiece and the robot end-effector is significant, models generated purely by point cloud fusion may exhibit alignment errors with the physical object. By leveraging the spatial relationship between the AprilTag and the point cloud model, the system can more accurately estimate the pose of the workpiece. This approach

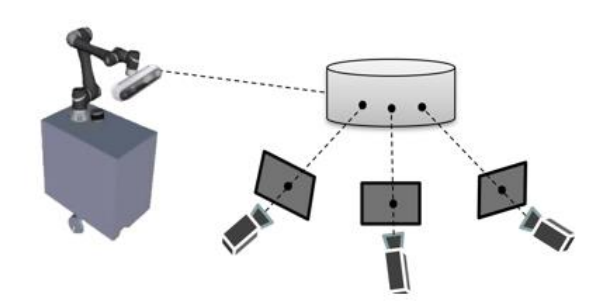


Fig. 3. Schematic of multi-view sampling of a mobile robot, with the target object (white cylinder) and camera poses (dashed lines).

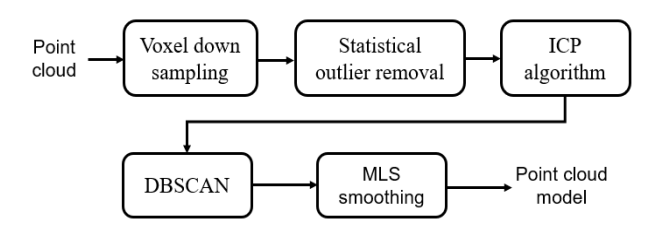


Fig. 4. Flow chart of point cloud modeling.

integrates feature-based referencing with point cloud spatial data, improving the accuracy and robustness of object localization through the use of transformation matrices.

#### B. Object Model Reconstruction and Segmentation

In order to build a complete point cloud model, after obtaining multiple point cloud data and their corresponding transformation matrices, these point clouds are fused into a complete model. The flowchart is shown in Fig. 4. It includes cloud pre-processing, ICP registration, segmentation and model post-processing. In the point cloud preprocessing part, voxel down sampling is first used to reduce the point cloud density, accelerate subsequent calculations and reduce the computational burden, while retaining the main geometric features of the point cloud. Since point clouds often contain noise and outliers during the sampling process, the statistical outlier removal method is used to remove noise and improve the accuracy of the final reconstruction. After point cloud pre-processing, the ICP algorithm in Open3D [11] is adopted to gradually align each point cloud to a unified coordinate system. Since the initial transfer matrix is required to assist in alignment when ICP registers point clouds, the point cloud is aligned to a unified coordinate system by reading the corresponding transfer matrix saved between the reference marker when sampling the point cloud, and the point-to-plane ICP method is used to accurately align the point clouds, as shown in Fig. 5.

Iterative operations calculate optimal the rigid transformation matrix based on the distance between the nearest points to accurately align the point cloud; when ICP fails to converge, it provides a mechanism to retain the initial transformation to avoid error expansion due to failure to converge. After the point cloud is aligned, the algorithm merges the point cloud of each perspective with the reference point cloud in turn. The final point cloud model contains point cloud information from different perspectives, which can more comprehensively describe the geometry of the target object, thereby achieving accurate alignment and reconstruction of multi-perspective point clouds. Finally, in order to separate the

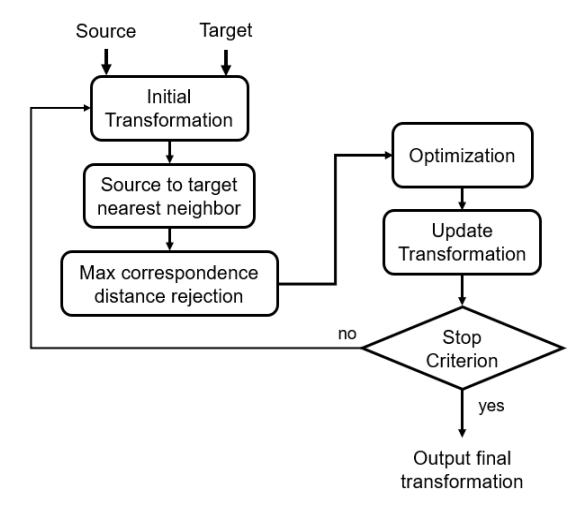


Fig. 5. ICP point cloud alignment algorithm.

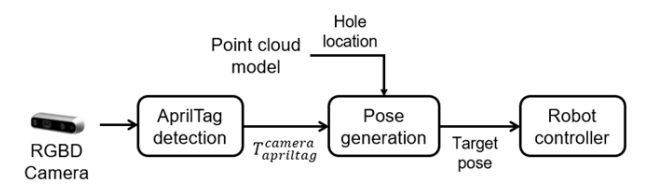


Fig. 6. Workflow of the piercing task using the mobile manipulator.

object model independently, DBSCAN is used for clustering, which automatically determines the number of clusters based on the spatial density of the points for grouping, and marks outliers as noise points for deletion. After completing the clustering of the point cloud, MLS [11] surface smoothing is performed, and finally the complete point cloud model is output.

### IV. POINT CLOUD-BASED ROBOTIC HOLE-PIERCING

After completing multi-view sampling and constructing the point cloud model of the workpiece, the proposed approach utilizes the generated point cloud as the basis for executing piercing tasks. To ensure that the manipulator can accurately localize and perform the subsequent piercing operations, AprilTag technology is employed to mark the workpiece and identify its pose. This allows the manipulator to establish the spatial relationship with the workpiece, locate the target positions, and carry out the piercing task accordingly. The workflow is illustrated in Fig. 6.

During the experiment, AprilTag are utilized as reference markers for localizing the piercing points, enabling the manipulator to perform piercing tasks at predefined hole locations on the workpiece model. First, hand-eye calibration is conducted to obtain the transformation matrix  $T_{camera}^{base}$ , which defines the spatial relationship between the robot base and the camera. Next, the camera detects the AprilTag attached to the workpiece and derives the transformation  $T_{apriltag}^{camera}$ . Additionally, during the point cloud model generation, the positional information of the AprilTag is integrated with the point cloud data, resulting in the transformation  $T_{PC \, model}^{AprilTag}$ . Based on these transformations, the overall transformation from the point cloud model to the robot base, denoted as  $T_{PC \, model}^{base}$ , can be computed, as shown in (1).

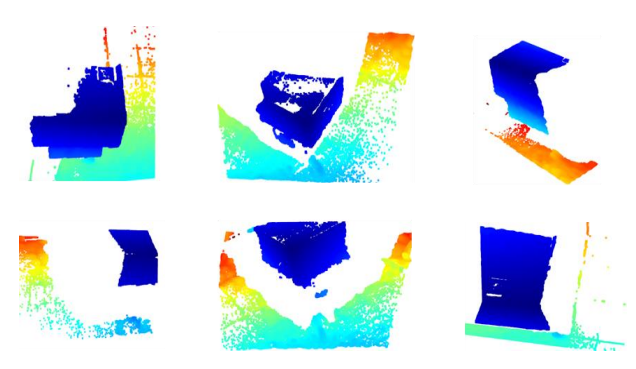


Fig. 7. Multi-view point cloud sampling data at different viewing angles for workpiece 1.

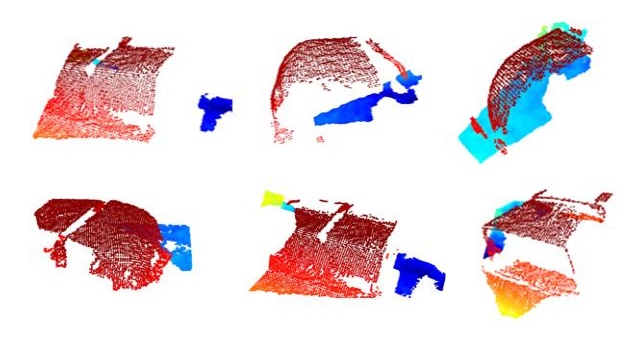


Fig. 8. Multi-view point cloud sampling data at different viewing angles for workpiece 2.

$$T_{\rm PC\ model}^{base} = T_{camera}^{base} T_{\rm AprilTag}^{\rm Camera} T_{\rm PC\ model}^{\rm AprilTag} \tag{1}$$

$$P_{base} = T_{\text{PC model}}^{base} {}^{-1}P_{\text{PC model}}$$
 (2)

Using the transformation  $T_{\rm PC\ model}^{base}$ , the pose  $P_{\rm PC\ model}$  of the point cloud model can be converted into the base coordinate frame, yielding  $P_{base}$ , as shown in (2). This transformation enables the manipulator to align accurately with the point cloud model, determine the pose of the workpiece, and carry out piercing during the piercing task.

After obtaining the relationship between the workpiece and the manipulator, the system first constructs a complete point cloud model of the workpiece through multi-view sampling to enable piercing. This model provides three-dimensional geometric information of the workpiece, including the spatial distribution of the point cloud coordinates. By using the 3D coordinates of the point cloud at the workpiece's vertices, information about the piercing plane can be obtained.

In this study, a hole-piercing experiment was conducted at the center of the plane. By acquiring the coordinates of the four vertices on the workpiece plane, the center point of the four vertices is calculated to determine the 3D spatial coordinates of the plane center for piercing purposes. When the manipulator performs the hole-piercing operation, it must adjust its orientation to match the posture of the workpiece plane.

To simplify the setting of rotation angles, the system uses the normal direction provided by AprilTag as a reference, assuming that the surface normal vector of the workpiece is aligned with the Z-axis direction of the AprilTag. Therefore, after marker detection and spatial calibration are completed, the posture of the manipulator can be directly set based on the orientation defined by the AprilTag. The direction perpendicular to the tag

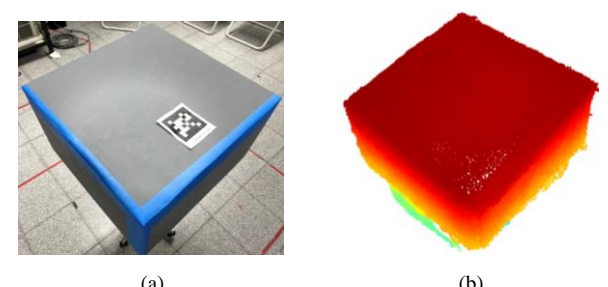


Fig. 9. Workpiece 1 (a) original, (b) point cloud model

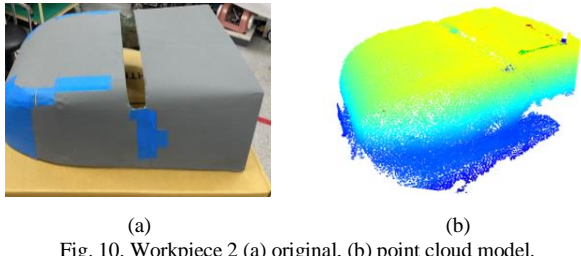


Fig. 10. Workpiece 2 (a) original, (b) point cloud model.

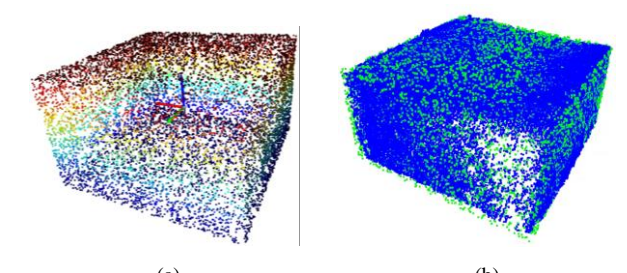


Fig. 11. Workpiece 1 (a) pint cloud converted from CAD model, (b) point cloud model after ICP registration.

surface is used as the tool's piercing direction, eliminating the need for additional estimation of the workpiece surface normal.

#### V.EXPERIMENTAL RESULTS

# A. Multi-View 3D Modeling Experiment

In order to verify the effectiveness of the proposed method for modeling point cloud objects, a box-shaped workpiece was selected and its actual length, width and height were measured to draw a CAD model. The point cloud images of workpiece 1, captured from different camera perspectives, are shown in Fig. 7. Similarly, the point cloud images of workpiece 2 from various viewpoints are presented in Fig. 8. The reconstructed model of workpiece 1 is illustrated in Fig. 9, while the model of workpiece 2 is shown in Fig. 10. Finally, the two are aligned through the ICP method to match the error, and the registration result is shown in Fig. 11. Fig. 11(a) is the established CAD model, and Fig. 11(b) is the registration result of the two models. The blue part in Fig. 11(b) shows the point cloud model of multi-perspective modeling, and the green part shows the CAD model and calculates the registration error of the two models. The root mean square error (RMSE) after registration is 7.84 mm. Since workpiece 2 does not have a CAD model, no error analysis was performed for this workpiece.

# B. Experimental Result of Robotic Piercing Task

In the experiment, the manipulator uses its end-effector gripper to grasp a tool and perform piercing actions at the holes





(a) (b) Fig. 12. Workpiece 1: (a) lying flat, (b) tilted 30 degrees.





Fig. 13. Workpiece 2: (a) lying flat, (b) tilted 30 degrees.

Table I. Piercing Accuracy for Workpiece 1 of Fig. 12(a)

| Test<br>No. |       | GT    |       | Estimation |       |       |       |       | Error |              |  |
|-------------|-------|-------|-------|------------|-------|-------|-------|-------|-------|--------------|--|
| 110.        | x(cm) | y(cm) | z(cm) | x(cm)      | y(cm) | z(cm) | x(cm) | y(cm) | z(cm) | Distance(cm) |  |
| 1           | 24.25 | 24.00 | 0.00  | 24.79      | 24.33 | -0.21 | 0.54  | 0.33  | 0.21  | 0.67         |  |
| 2           | 24.25 | 24.00 | 0.00  | 25.14      | 24.51 | -0.03 | 0.89  | 0.51  | 0.03  | 1.03         |  |
| 3           | 24.25 | 24.00 | 0.00  | 24.91      | 24.41 | -0.09 | 0.66  | 0.41  | 0.09  | 0.78         |  |
| 4           | 24.25 | 24.00 | 0.00  | 24.06      | 24.17 | -0.17 | 0.19  | 0.17  | 0.17  | 0.31         |  |
| 5           | 24.25 | 24.00 | 0.00  | 24.97      | 24.46 | 0.08  | 0.72  | 0.46  | 0.08  | 0.86         |  |
| 6           | 24.25 | 24.00 | 0.00  | 25.04      | 24.25 | -0.21 | 0.79  | 0.25  | 0.21  | 0.85         |  |
| 7           | 24.25 | 24.00 | 0.00  | 24.82      | 24.36 | -0.19 | 0.57  | 0.36  | 0.19  | 0.70         |  |
| 8           | 24.25 | 24.00 | 0.00  | 25.03      | 24.22 | -0.07 | 0.78  | 0.22  | 0.07  | 0.81         |  |
| 9           | 24.25 | 24.00 | 0.00  | 25.02      | 24.31 | -0.15 | 0.77  | 0.31  | 0.15  | 0.84         |  |
| 10          | 24.25 | 24.00 | 0.00  | 25.14      | 24.46 | -0.12 | 0.89  | 0.46  | 0.12  | 1.01         |  |
| Avg. Err.   |       |       |       |            |       |       |       |       |       | 0.79         |  |
| Std. Dev.   |       |       |       |            |       |       |       |       |       | 0.19         |  |

Table II. Piercing Accuracy for Workpiece 1 of Fig. 12(b)

| Test<br>No. | GT    |       |       | Estimation |       |       |       | Error |       |              |
|-------------|-------|-------|-------|------------|-------|-------|-------|-------|-------|--------------|
|             | x(cm) | y(cm) | z(cm) | x(cm)      | y(cm) | z(cm) | x(cm) | y(cm) | z(cm) | Distance(cm) |
| 1           | 24.25 | 24.00 | 0.00  | 25.01      | 24.21 | -0.21 | 0.76  | 0.21  | 0.21  | 0.82         |
| 2           | 24.25 | 24.00 | 0.00  | 24.92      | 24.32 | -0.14 | 0.67  | 0.32  | 0.14  | 0.76         |
| 3           | 24.25 | 24.00 | 0.00  | 25.03      | 24.15 | -0.27 | 0.78  | 0.15  | 0.27  | 0.84         |
| 4           | 24.25 | 24.00 | 0.00  | 24.63      | 24.31 | -0.09 | 0.38  | 0.31  | 0.09  | 0.50         |
| 5           | 24.25 | 24.00 | 0.00  | 25.1       | 24.27 | 0.15  | 0.85  | 0.27  | 0.15  | 0.90         |
| 6           | 24.25 | 24.00 | 0.00  | 24.83      | 24.31 | 0.21  | 0.58  | 0.31  | 0.21  | 0.69         |
| 7           | 24.25 | 24.00 | 0.00  | 25.02      | 24.46 | -0.22 | 0.77  | 0.46  | 0.22  | 0.92         |
| 8           | 24.25 | 24.00 | 0.00  | 25.11      | 24.22 | -0.14 | 0.86  | 0.22  | 0.14  | 0.90         |
| 9           | 24.25 | 24.00 | 0.00  | 24.98      | 24.51 | -0.27 | 0.73  | 0.51  | 0.27  | 0.93         |
| 10          | 24.25 | 24.00 | 0.00  | 25.04      | 24.41 | 0.09  | 0.79  | 0.41  | 0.09  | 0.89         |
| Avg. Err.   |       |       |       |            |       |       |       |       |       | 0.82         |
| Std. Dev.   |       |       |       |            |       |       |       |       | 0.13  |              |

on the workpiece, with the piercing positions recorded accordingly. The piercing experiments in this study are divided into four parts, involving two types of workpieces: a box-shaped workpiece and a robot body shell. Each workpiece is tested in two orientations—lying flat and tilted at a 30-degree angle.

For the box-shaped workpiece, the piercing position is determined based on the point cloud model obtained from previous modeling. The coordinates of the four corner vertices are extracted, and the center point is calculated from these vertices to define the piercing location. In the case of the robot shell, since the front surface of the workpiece is a curved surface, it is not feasible to define the center point by selecting four corners. Instead, the midpoint of a groove on the workpiece is selected. The position of this point is measured on the model

Table III. Piercing Accuracy for Workpiece 2 of Fig. 13(a)

| Test<br>No. |                        | GT    |       | Estimation |       |       | Error |       |       |              |  |
|-------------|------------------------|-------|-------|------------|-------|-------|-------|-------|-------|--------------|--|
|             | x(cm)                  | y(cm) | z(cm) | x(cm)      | y(cm) | z(cm) | x(cm) | y(cm) | z(cm) | Distance(cm) |  |
| 1           | 22.00                  | 29.50 | 0.00  | 22.38      | 30.16 | -0.07 | 0.38  | 0.66  | 0.07  | 0.76         |  |
| 2           | 22.00                  | 29.50 | 0.00  | 22.64      | 29.57 | -0.21 | 0.64  | 0.07  | 0.21  | 0.68         |  |
| 3           | 22.00                  | 29.50 | 0.00  | 22.37      | 29.94 | 0.09  | 0.37  | 0.44  | 0.09  | 0.58         |  |
| 4           | 22.00                  | 29.50 | 0.00  | 22.97      | 29.54 | -0.21 | 0.97  | 0.04  | 0.21  | 0.99         |  |
| 5           | 22.00                  | 29.50 | 0.00  | 23.12      | 29.44 | -0.14 | 1.12  | 0.06  | 0.14  | 1.13         |  |
| 6           | 22.00                  | 29.50 | 0.00  | 22.31      | 28.88 | 0.21  | 0.31  | 0.62  | 0.21  | 0.72         |  |
| 7           | 22.00                  | 29.50 | 0.00  | 22.43      | 29.9  | -0.17 | 0.43  | 0.4   | 0.17  | 0.61         |  |
| 8           | 22.00                  | 29.50 | 0.00  | 22.74      | 29.73 | 0.15  | 0.74  | 0.23  | 0.15  | 0.79         |  |
| 9           | 22.00                  | 29.50 | 0.00  | 22.64      | 28.93 | -0.22 | 0.64  | 0.57  | 0.22  | 0.88         |  |
| 10          | 22.00                  | 29.50 | 0.00  | 22.87      | 29.17 | 0.31  | 0.87  | 0.33  | 0.31  | 0.98         |  |
|             | Avg. Err.<br>Std. Dev. |       |       |            |       |       |       |       |       | 0.81         |  |
|             |                        |       |       |            |       |       |       |       |       | 0.18         |  |

Table IV. Piercing Accuracy for Workpiece 2 of Fig. 13(b)

| Test<br>No. |                        | GT    |       | 1     | Estimatio | n     | Ептог |       |       |              |
|-------------|------------------------|-------|-------|-------|-----------|-------|-------|-------|-------|--------------|
|             | x(cm)                  | y(cm) | z(cm) | x(cm) | y(cm)     | z(cm) | x(cm) | y(cm) | z(cm) | Distance(cm) |
| 1           | 22.00                  | 29.50 | 0.00  | 22.51 | 30.12     | -0.19 | 0.51  | 0.62  | 0.19  | 0.82         |
| 2           | 22.00                  | 29.50 | 0.00  | 22.63 | 29.97     | -0.07 | 0.63  | 0.47  | 0.07  | 0.79         |
| 3           | 22.00                  | 29.50 | 0.00  | 21.25 | 29.76     | -0.15 | 0.75  | 0.26  | 0.15  | 0.81         |
| 4           | 22.00                  | 29.50 | 0.00  | 22.9  | 29.54     | -0.21 | 0.9   | 0.04  | 0.21  | 0.93         |
| 5           | 22.00                  | 29.50 | 0.00  | 22.45 | 29.32     | -0.14 | 0.45  | 0.18  | 0.14  | 0.50         |
| 6           | 22.00                  | 29.50 | 0.00  | 22.44 | 29.55     | -0.36 | 0.44  | 0.05  | 0.36  | 0.57         |
| 7           | 22.00                  | 29.50 | 0.00  | 22.93 | 28.87     | -0.17 | 0.93  | 0.63  | 0.17  | 1.14         |
| 8           | 22.00                  | 29.50 | 0.00  | 22.45 | 29.88     | 0.38  | 0.45  | 0.38  | 0.38  | 0.7          |
| 9           | 22.00                  | 29.50 | 0.00  | 22.72 | 29.64     | -0.89 | 0.72  | 0.14  | 0.89  | 1.15         |
| 10          | 22.00                  | 29.50 | 0.00  | 22.69 | 30.08     | -0.46 | 0.69  | 0.58  | 0.46  | 1.01         |
|             | Avg. Err.<br>Std. Dev. |       |       |       |           |       |       |       |       |              |
|             |                        |       |       |       |           |       |       |       |       |              |

and designated as the target point for the manipulator to perform the piercing operation.

In this study, the aforementioned method is used to calculate the coordinates of the piercing point in the robot base frame, enabling the execution of the piercing operation. As shown in Fig. 12, the manipulator performs the piercing task on workpiece 1 based on predefined target points. Fig. 13 illustrates the manipulator executing a similar task on workpiece 2. The piercing experiment is repeated ten times, and the position of each piercing point is measured to calculate the positioning error.

Fig. 12(a) shows a screenshot of the experiment with Workpiece 1 in a flat position, while Fig. 12(b) presents the experiment with Workpiece 1 tilted 30 degrees. The corresponding experimental data are summarized in Tables I and II, respectively. Fig. 13(a) shows a screenshot of the experiment with Workpiece 2 in a flat position, while Fig. 13(b) presents the experiment with Workpiece 2 tilted 30 degrees. The corresponding experimental data are summarized in Tables III and IV, respectively.

#### VI. CONCLUSIONS

In this study, we developed a 3D modeling system for unknown large objects using a mobile robot. By equipping the mobile manipulator with an eye-in-hand depth camera and a base-mounted 3D LiDAR, the system is capable of performing multi-view point cloud data acquisition and fusing the data into a complete object model. The integration of ICP-based registration, outlier filtering, smoothing, and DBSCAN segmentation techniques improves the accuracy and completeness of the resulting 3D reconstruction. To validate the system, we conducted a hole-piercing experiment using

AprilTag markers to verify piercing accuracy based on the reconstructed object model. The results demonstrate the system's ability to effectively generate piercing paths and perform physical operations aligned with the point cloud model. This framework establishes a solid foundation for vision-based robotic applications in automated manufacturing, particularly in scenarios involving large, irregular, and previously unknown workpiece. In the future, we will enhance the quantitative performance of the system. Future work will also explore view planning strategies and real-time adaptability to further enhance modeling efficiency and robot-based machining.

# ACKNOWLEDGMENT

The authors would like to thank Industrial Technology Research Institute (ITRI) for the support of this research project.

#### REFERENCES

- H. Wu, T. Zou, H. Burke, S. King and B. Burke, "A novel approach for porcupine crab identification and processing based on point cloud segmentation," in Proc. 2021 20th International Conference on Advanced Robotics (ICAR), Ljubljana, Slovenia, 2021, pp. 1101-1108.
- G. Zhang, J. Wang, F. Cao, Y. Li and X. Chen, "3D curvature grinding [2] path planning based on point cloud data," in Proc. 2016 12th IEEE/ASME International Conference on Mechatronic and Embedded Systems and Applications (MESA), Auckland, New Zealand, 2016, pp. 1-6.
- [3] Point Cloud Library, Jul. 2020. [Online]. https://github.com/PointCloudLibrary/pcl Accessed on July, 2024.
- Harintaka Harintaka and Calvin Wijaya, "Automatic point cloud segmentation using RANSAC and DBSCAN algorithm for indoor model," Telecommunication Computing Electronic and Control, Vol. 21, No. 6, pp. 1317-1325, 2023.
- Alfan Rizaldy Pratama, Bima Sena Bayu Dewantara, Dewi Mutiara Sari, and Dadet Pramadihanto, "Improvement of DBSCAN algorithm involving automatic parameters estimation and curvature analysis in 3D point cloud of piled pipe," Journal of Image and Graphics, Vol. 12, No. 2, pp. 176-185, 2024.
- [6] M. Maboudi, M. Homaei, S. Song, S. Malihi, M. Saadatseresht and M. Gerke, "A review on viewpoints and path planning for UAV-based 3D reconstruction," IEEE Journal of Selected Topics in Applied Earth Observations and Remote Sensing, Vol. 16, pp. 5026-5048, 2023.
- B. Fei et al., "Comprehensive review of deep learning-based 3D point cloud completion processing and analysis," IEEE Transactions on Intelligent Transportation Systems, Vol. 23, No. 12, pp. 22862-22883,
- [8] Xin Wen, Peng Xiang, Zhizhong Han, Yan-Pei Cao, Pengfei Wan, Wen Zheng and Yu-Shen Liu, "PMP-Net: point cloud completion by learning multi-step point moving paths PMP-Net," in Proc. IEEE/CVF Conference on Computer Vision and Pattern Recognition (CVPR), Nashville, TN, USA, 2021, pp. 7443-7452.
- [9] W. Dubois, N. Samson, E. Daum, J. Laconte and F. Pomerleau, "Under Pressure: Altimeter-Aided ICP for 3D Maps Consistency," in Proc. 2025 IEEE International Conference on Robotics and Automation (ICRA), Atlanta, GA, USA, 2025, pp. 9370-9376.
- [10] D. Deng, "DBSCAN Clustering Algorithm Based on Density," in *Proc.* 7th International Forum on Electrical Engineering and Automation (IFEEA), Hefei, China, 2020, pp. 949-953.
- "Open3D: A Modern Library for 3D Data Processing," GitHub, [Online]. Available: https://github.com/isl-org/Open3D. Accessed on July 2024.



Chun-An Liu is currently working toward the M.S. degree in Electrical and Control Engineering at National Yang Ming Chiao Tung University, Hsinchu, Taiwan. His current research interests include autonomous robotic modeling of unknown objects, multi-view 3D reconstruction, robotic perception and planning.



Chih-Hsien Yen received the B.S. degree in Mechanical and Electromechanical Engineering from National Sun Yat-sen University, Kaohsiung, Taiwan, in 2023. He is currently working toward the M.S. degree in Electrical and Control Engineering at National Yang Ming Chiao Tung University, Hsinchu, Taiwan. His current research interests are in the areas of robotics and embodied intelligence.



Hong-Xian Wu is currently working toward the M.S. degree in Electrical and Control Engineering at National Yang Ming Chiao Tung University, Hsinchu, Taiwan. His current research interests include robotics, mobile robots and obstacle avoidance.



Kai-Tai Song received his B.S. degree in power mechanical engineering from National Tsing Hua University, Taiwan in 1979 and Ph.D. degree in mechanical engineering from Katholieke Universiteit Leuven, Belgium in 1989. Since 1989, he has been on the faculty and is currently a distinguished professor of Institute of Electrical and Control Engineering, Department of Electronics and Electrical Engineering, National Yang Ming Chiao Tung University (NYCU), Taiwan. His research interests include motion planning

of collaborative robots, autonomous mobile robot, robotic vision and mobile manipulation.



Chin-Chi Hsiao received the Ph.D. degree in mechanical engineering from National Chiao Tung University (NCTU), Taiwan. He is currently with the Mechanical and Mechatronics Systems Research Laboratories, Industrial Technology Research Institute (ITRI), Taiwan.